Journal of Materials Chemistry A

Accepted Manuscript

ROYAL SOCIETY OF CHEMISTRY

www.rsc.org/materialsA

Interconnected TiOx/carbon hybrid framework incorporated silicon for stable lithium ion battery anodes

Ming-Shan Wang, Wei-Li Song and Li-Zhen Fan*

Institute of Advanced Materials and Technology, University of Science and Technology Beijing, Beijing, 100083, China

*Corresponding author: E-mail: Tel./fax: +86-10-62334311; fanlizhen@ustb.edu.cn.

Abstract

Silicon is one of the most promising anode materials for lithium ion batteries due to its high-specific capacity. However, its poor cycling stability and rate capability limit its practical use. Herein, we report scalable fabrication of unique three-dimensional porous silicon/TiO_x/carbon (Si/TiO_x/C, $0<x<2$) binder free composite electrode for lithium ion batteries. The TiO_x/C frameworks were incorporated by a slurry coating method followed by heat treatment, resulting in well-connected three dimensional framework structure consisting of Si nanoparticles conformably embedded in conducting TiO_x/C matrix. The porous TiO_x/C conductive framework effective alleviates the volume change of Si during cycling and substantially improves the structural stability of electrode materials. Moreover, the amorphous TiO_x/C conductive matrix provides high electrical conductivity and electrochemical reaction between Li and Si. As a consequence, the Si/TiO_x/C exhibits a stable reversible specific capacity of 1696 mAh g^{-1} at 0.1 A g^{-1} after 100 cycles with 87% capacity retention, and superior rate capability (754 mAh g^{-1} at 15 A g^{-1}). The exceptional performance of Si/TiO_x/C electrode combined with the facile synthesis technique makes it promising for high energy lithium ion batteries.

Keywords: Lithium ion battery; Silicon; Titanium oxide; Carbon

1. Introduction

Lithium-ion batteries (LIBs) have been employed successfully in various electronic devices for the past two decades and the types of applications are currently expanding to electric vehicle and energy storage systems. In recent years, Si has become a powerful candidate as an anode material for LIBs to replace the conventional graphite anode, due to the demand for high energy and power density. It is well-known that Si has the highest theoretical capacity (4200 mAh g^{-1}), low Li-uptake voltage (0.4-0.5 V vs Li/Li^+), abundant and environmentally benign nature[1-3]. However, practical application of Si has been hindered by its crucial disadvantages as anode material. Firstly, although the Si anodes deliver high specific capacity, they suffer from a large volume change of up to 300% during repeated cycling, which leads to stress-induced cracking and poor cycle life. On the other hand, the unstable SEI film at the interface between Si and the liquid electrolyte also reduces lithium diffusivity and causes irreversible capacity loss[4].

To address those issues, various strategies have been developed to tackle interfacial and structural instability problems of Si caused by volume change, such as optimizing particle size[5, 6] or morphology[7-14], and designing silicon/carbon hybrids[15-25]. Among all those strategies, dispersing silicon in carbonaceous materials have attracted significant interest because carbon matrix can efficiently enhance the electrical conductivity of Si and form a stable SEI layer, which results in improved electrochemical performances[20, 26, 27]. However, concerns on the safety issue resulted from the undesirable exothermic behavior still exist for silicon-carbon composites[28]. Moreover, the energy density of those silicon-carbon composite remains well below that of pure silicon. Rather than dispersing silicon nanoparticles in carbonaceous materials, titanium dioxide (TiO_2) has been proposed as a prospective candidate for the conductive materials of Si electrode material for LIBs[28-35]. On the one hand, TiO_2 exhibits a low volume expansion (<4%) during the lithiation/delithiation process, which can provide a mechanical support of Si[36]. On the other hand, the higher working voltage of TiO_2 anode (higher than 1.5 V vs. Li/Li^+) can efficiently eliminates the formation of SEI layers and lithium plating on the anode, which improves the safety of the batteries

as compared with its carbon-based counterparts. Many synthetic strategies have been reported for Si/TiO_2 hybrid nanostructures, such as Si/TiO_2 nanotube[30, 32-34], Si/TiO_2 nanowires[28, 29, 35, 37], porous Si/TiO_2 nanoparticles[31, 38, 39]. Those pioneering works have demonstrated that rigid TiO_2 can suppress the disintegration of the Si nanoparticles undergoing repeated volume change during cycling and thereby improve the cycle performance. Meanwhile, a robust TiO_2 shell enhances thermal stability of the Si composites, which can prevent possible thermal runaway and safety problems of the cells. Despite the advantages, rutile-type and anatase-type TiO_2 has limited Li^+ ion diffusion coefficient (10^{-11} to 10^{-13} cm s^{-1})[40] and the low electronic conductivity (10^{-4} S·cm^{-1}) [41], which limits the Si based materials as a potential high power anode material. According to previous study, optimize the crystalline structure of TiO_2[42-44] and introduction of oxygen-deficient[45] could shorten the Li ion diffusion and charge transfer, which achieve high power density of batteries.

In order to obtain high rate performance of electrode materials, maximizing both electronic conductivity and mechanical stability of composites are the key requirements. Taking advantages of the high electronic conductivity of carbon and excellent mechanical and thermal stability property of TiO_2, herein, we report unique three-dimensional porous silicon/TiO_x/carbon (Si/TiO_x/C, $0<x<2$) composite electrode, in which silicon nanoparticles were homogeneously dispersed in mesoporous TiO_x/C conductive matrix by a simple hydrolysis process combined with slurry coating method and heat treatment. The triblock poly (propylene oxide)-poly (ethylene oxide)-poly-(propylene oxide) copolymers (P123) are used as templates in the presence of the carbon and TiO_x precursor by self-assembly, achieving uniform porous structures. Then, the organic block copolymer component is removed after formation of the structure by calcination, thereby generating mesoporous structure.[46] This electrode can be easily obtained by pasting the mixture of silicon, TiO_2 precursor, and carbon precursor onto a copper foil substrate. Encapsulation of Si nanoparticles inside a porous robust TiO_x/C composite scaffold effectively suppresses the disintegration of the Si nanoparticles during repeated cycling and thereby improves the cycle performance. Meanwhile, polycrystalline TiO_2 was formed in the low temperature which provides an enhanced electrical conductivity for the

electrochemical reaction between Li and Si. Moreover, the electrode fabrication process is highly compatible with the current industrial techniques for electrodes of lithium ion batteries, which are simple, mature and low-cost.

2. Experimental Material and methods

2.1 preparation of porous Si/TiO_x/C composite electrode

Typically, 0.3 g of Si nanoparticles (Si NPs, Xuzhou Jiechuang New Material Technology Co., 30-50 nm) was dispersed in 5 mL of N, N-dimethylformamide (DMF) to form a homogeneous suspension, followed by adding 0.3 g of P123, (average Mn~5,800, Simga-Aldrich) into the above suspension under vigorous stirring for 30 min. Then 0.895 g tetrabutyl titanate ($Ti(OC_4H_9)_4$, TBOT), 0.27 g H_2O and 0.298g triethanolamine were added to the suspension with vigorous stirring. After slow hydrolysis for 12 hours, the TiO_2 shell was deposited on the Si NPs. Then 0.3 g polymethyl methacrylate (PMMA) were added and stirred for 1 h to achieve uniform slurry which was then coated on Cu current collector. After aging at 50 °C for 10 h, the Si/TBOT/PMMA composite was calcined at 400°C for 5 h under flowing nitrogen to obtain the final Si/TiO_x/C composite electrode. In order to compare the electrochemical performance of nanocomposites, the Si/C nanocomposite (mixed with 0.3 g Si and 0.3 g PMMA) was synthesized with the same experimental procedure. The Si/TiO_x was also synthesized by coating TiO_x on the Si nanoparticles by hydrolysis of TBOT as the same experimental procedure.

2.2 Characterization

The X-ray diffraction (XRD) patterns were recorded on a Rigaku D/max-RB diffractometer using Cu Kα radiation (40 kV, 30 mA), with a step of 0.02^o between 10^o and 90^o. The morphology and structure were analyzed by a field emission scanning electron microscope (FESEM, JEOL JSM-6330). Transmission electron microscopy (TEM), high-resolution TEM (HRTEM) images, the selected-area electron diffraction (SAED) pattern, elemental mapping were conducted on a transmission electron microscopy (TEM, JEOL JEM-2010). Thermogravimetric analysis (TGA) was carried out with a TGA/DSC1 type instrument (Mettler Toledo, Switzerland) from 50 to 600 ^{o}C with

a heating rate of 10 ^{o}C min^{-1} in air. X-ray photoelectron spectroscopy (XPS) analysis was performed on a K-alpha (Thermo Fisher Scientific, Escalab 250xi). The Brunauer-Emmett-Teller (BET) test was determined via a Quantachrome Autosorb-IQ2 nitrogen adsorption apparatus at 77K after being degassed at 300 ^{o}C for at least 3 h. Pore size distribution plot was obtained by the Barrett-Joyner-Halenda (BJH) method. After cycling at constant current density, the electrode was carefully disassembled from the cell and then rinsed with dimethyl carbonate in an Ar-filled glovebox to remove residual electrolyte. Then the electrodes were dried under vacuum for 3 h and transferred to chamber of FESEM and HRTEM equipment. The morphology change and crystalline structure of electrodes after cycling were analyzed by FESEM and HRTEM system.

Electrochemical performance was performed under ambient temperature using two-electrode 2032 coin-type cell. The prepared Si/TiO_x/C composite electrodes were punched into circular with a diameter of 1.4 cm to be used as the working electrodes without binder, in which the mass of the active material was approximately 0.5-1.5 mg. Metal lithium foil was used as the counter electrodes. Celgard 2400 membrane served as the separator and a solution of 1M $LiPF_6$ in ethylene carbonate (EC), ethyl methyl carbonate (EMC) and dimethyl carbonate (DEC) (1:1:1, in volume) was used as the electrolyte. The Si/C working electrodes were fabricated by dispersing active materials (80 %), carbon black (10 %), and PVDF (10 %) in N-methylpyrrolidinone to form slurry, which was uniformly spread on Cu foil current collector. The CR2032 coin-type cells were assembled in an argon-filled glove box. Electrochemical workstation (CHI660) was used to study the cyclic voltammetry (CV) performance in the potential range of 0.01-3.0 V at a scan rate of 0.1 mV s^{-1}. Electrochemical impedance spectroscopy (EIS) was measured in the frequency between 100 kHz and 0.01 Hz and the amplitude was 5 mV. The discharge and charge measurements of the batteries were performed on the battery test system (LAND CT2001A, Wuhan Jinnuo Electronics, Ltd.) in the fixed voltage window between 0.01 and 3.0 V at room temperature. The capacities of electrodes are based on the weight of total active materials weight.

3. Results and discussion

The unique 3D hybrid porous Si/TiO_x/C composite electrode is prepared by a simple hydrolysis method combined with slurry coating method. Figure 1 showed the fabrication procedure. In brief, TiO_x precursor was firstly coated on the surface of Si NPs to form a uniform shell via hydrolysis of TBOT. Then, the Si/TBOT was homogeneously mixed with PMMA to form a yellow suspension. The suspension was rapidly cross-linked after stirring, obtaining a viscous slurry which was then bladed onto a copper foil current collector and heated at 400°C to form binder free Si/TiO_x/C composite electrode. The porous TiO_x/C conductive framework can provide an enhanced electrical conductivity for the electrochemical reaction between Li and Si. Meanwhile, porous framework can also suppress the disintegration of the Si nanoparticles undergoing repeated volume change during cycling, thereby improving the cell performance. Moreover, this solution-based synthesis method and its compatibility coating method make this system readily scaled up for electrode[47].

Figure 2 showed FESEM images of the Si/TiO_x/C composite electrode. Typically, the spherical Si NPs have an average diameter of 50 nm (Figure 2a), while there is no obvious Si NPs observed in Figure 2b. Compared with Si/TBOT/PMMA, the surface morphology of Si/TiO_x/C composite electrode is rougher after heat treatment (Figure 2c and 2d). Abundant pores exist in the matrix due to the removal of P123. However, no pronounced Si NPs exposed on the surface of matrix, indicating that the Si NPs are well encapsulated in the three dimensional matrix.

The phase composition and chemical bonding environment of the as-prepared composite electrode were further examined by XRD patterns and XPS spectra. From the XRD patterns of the samples shown in Figure 3, Si, Si/C and Si/TiO_x/C have the major identified peaks at 2θ= 28.3, 47.3, 56.0, 69.1, 76.3°, indexed as (111), (220), (311), (400), and (331) planes of cubic silicon (JCPDS #27-1402), respectively. There is not any other peak corresponding to the graphite in the pattern of Si/C and Si/TiO_x/C, which is most likely due to the formation of the amorphous structure of carbon at low temperature. It is also noted that no significant TiO_X peaks observed in the pattern of Si/TiO_x/C, indicating that the formation of nanocrystal TiO_X at low temperature treatment[48]. XPS

was further employed to gain insight into the electronic properties of Ti, Si, O, and C atoms within Si/TiO_x/C (Fig.3b). In addition to the peaks of Si, O, C elements, Ti 2p peak can be observed in the full spectra of Si/TiO_x/C (Fig.3c). Although Si/TiO_x/C showed typical Ti $2p_{3/2}$ core-level XPS spectra with Ti^{4+} characteristics (Ti $2p_{3/2}$ peak at 458.7 eV of binding energy), it also exhibited a shoulder near 457.7 eV, which is characteristic of Ti^{3+}. The percentages of Ti^{4+} and Ti^{3+} are calculated to be 97.6% and 2.4%, assumed to be $TiO_{1.988}$. The results indicated that the component of Si/TiO_x/C is silicon, carbon and TiO_x, which is accordance with the reported literature[28, 29]. The existence of Ti^{3+} may come from the defects generated in TiO_2 structure which is due to partial oxygen loss leading to reduction and vacancy in inert atmosphere. The O 1s signal for Si/TiO_x/C is shown in Fig. 3d, indicating a peak at 530.2 eV and a shoulder located at a binding energy of 531.9 eV. The O 1s peak at 531.9 eV is in agreement with the reported O 1s binding energy of the Si-O-Ti species, which reflects the bonding of TiO_x to the surface of the Si NPs[49]. For quantifying the amount of amorphous carbon and TiO_{2-x} in the sample of Si/TiO_x/C, TGA was carried out in air (Fig. S1). The weight loss below 200 ^oC results from the evaporation of water in sample. The weight loss at 200-500 ^oC could be mainly attributed to the removal of the carbon. Thus, the concentration of carbon in Si/TiO_x/C is calculated to be about 23 wt.%. The concentration of Si in Si/TiO_x/C was determined by the concentration of Si in Si/TBOT (Table S1). Since the hydrolysis reaction of TBOT was completed in the experiment, the theoretical weight percentage of Si in Si/TiO_x was 45 %. Combined with the TGA curves, the concentration of Si, TiO_x and carbon in Si/TiO_x/C is 34%, 43%, 23%, respectively.

Nitrogen adsorption and desorption measurements were carried out for Si/TiO_x/C. The total surface area and total pore volume for Si/TiO_x/C are calculated to be 130.93 $m^2\ g^{-1}$ and 0.4704 $cm^3\ g^{-1}$. Furthermore, the adsorption-desorption isotherm of Si/TiO_x/C exhibits the typical type IV nitrogen adsorption branch with a H_2 hysteresis loop, which is characteristic of a mesoporous structure (Figure 4a). The pore size distribution calculated by the BJH method derived from the desorption branch is around 3.8 nm (Figure 4b). The mesopores should originate from the removal of P123. The presence of mesopores in the matrix allows electrolytes for easier and faster penetration,

thus facilitating electrolyte and ion diffusion from/to Si.

To investigate electrochemical performance of the Si/TiO_x/C composite electrode as an anode material for LIBs, the composite was directly used as working electrode and lithium foil was employed both as reference and counter electrodes. Figure 5a depicts the voltage profiles of Si/TiO_x/C film electrode during galvanostatic charge (delithiation)-discharge (lithiation) in a voltage window of 0.01-3 V vs. Li/Li^+ at a current density of 100 mA g^{-1}. It is noted that a long voltage plateau locates at around 0.1 V for discharge curves, which represent phase transformation of crystalline Si into amorphous Li_xSi. There is no pronounced plateau around 1.7 V for Si/TiO_x/C, which means the main discharge/charge reaction is based on alloying/dealloying between Li and Si[28, 31]. Constant-current measurements of identically prepared TiO_x/C are included in Figure S2, which also shows the same plateau features as Si/TiO_x/C. For the first charge curve of Si/TiO_x/C, it exhibits a single and flat plateau at about 0.4 V, corresponding to the two-phase reaction from crystalline $Li_{15}Si_4$ to amorphous Li_xSi.[50] In the first cycle, the Si/TiO_x/C exhibits initial discharge and charge capacities of 2600 and 1946 mAh g^{-1}, respectively, with a coulombic efficiency (CE) of 74.8%. The CE in the first cycle is higher than those of other Si electrodes in which Si directly coated with TiO_2 or carbon[31, 51, 52], implying the importance of the encapsulation of Si NPs within three dimensional conductive matrixes for stable SEI formation. Most importantly, Si/TiO_x/C exhibits decent capacity retention for a large number of cycles. After arriving at a stabilized capacity value within initial 10 cycles, the Si/TiO_x/C exhibits excellent cycling stability and almost invariably achieves a capacity of ca. 1696 mAh g^{-1} and 87 % of the original capacities are retained after 100 cycles. For comparison, the cycling performances of Si/C are exhibited in Figure 5b as well. Although it indicates an activation process in the initial cycle, it presents much poor cycle performance, only delivering a capacity of 376 mA h g^{-1} after 100 cycles. The poor capacity retention of Si/C is attributed to the large volume expansion and shrinkage during the repeated cycling, which result in the unstable SEI layer formation. In addition, although the Si/TiOx exhibits high initial discharge and charge capacity of 3610 and 1767 mAh g^{-1}, it only maintains a reversible discharge capacity of 608 mAh g^{-1} after 10

cycles. The rapid capacity fade can be attributed to the expansion/contraction of silicon during the charge and discharge, which results in the disruption of the rigid TiOx shells and pulverization of Si nanoparticles. In comparison, encapsulation of Si inside porous TiO_x/C framework can alleviate the disintegration of the Si during the repeated volume change and thus increasing the structure stability. In addition, the oxygen-deficient TiO_x has narrower band gap, which can provide an enhanced electrical pathway of high conductivity for electrochemical reaction between Li and Si[53-55]. Meanwhile, a Li_xTiO_2 phase is formed during the lithiation reaction of Li and TiO_x, wihch acts as a passivating layer to promote the formation of stable SEI layer. As a result, the cycling performance of Si/TiO_x/C electrode is significantly improved compared with bare Si and Si/C electrode[28, 29].

The cycling performance at different current densities of Si/TiOx/C with the voltage window of 0.01-3.0 V is also supplied in Figure S3. From the voltage profiles of Si/TiO_x/C, it can be also clearly seen that at the voltage above 1.5 V, there is a little lithium ion extraction from Si. As a result, the Si/TiO_x/C electrode obtains reversible capacities of 1046, 786, and 576 mAh g^{-1} at current densities of 0.2, 0.5, and 1 A g^{-1}. Although, the polarization of electrode at higher voltage window is significantly increased in the potential profiles of Si/TiOx/C (Figure S3a). In order to decrease the polarization of electrodes, the rate capability was carried at the voltage window of 0.01-1.5 V vs. Li/Li^+, as shown in Figure 5c. When the current density increases from 0.2 A g^{-1} to 15 A g^{-1}, the Si/TiO_x/C exhibits high capacity retention, as the specific capacity change from 1024 mAh g^{-1} to 754 mAh g^{-1}, respectively (Figure 5d). In particular, it is noteworthy that even when the current density increases 75 times (0.2 A g^{-1} to 15 A g^{-1}), 73.6% of the original capacity is still preserved. Even after cycling at such a high current rate, the capacity is recoverable as validated by the case at 0.2 A g^{-1}. On the other hand, Si/C exhibits charge capacities of 616 and 304 mA h g^{-1} when the current densities were increased from 0.2 to 5 A g^{-1} (Figure 5d). When the current is again reduced to that used in the first cycle after 90 cycles, the specific capacity of Si/TiO_x/C returned to 948 mAh g^{-1}, implying that the volume change of Si/TiO_x/C is quite reversible without pulverization. It is obvious that the rate capability of Si/TiO_x/C is significantly higher than that of Si/C. Table S2 lists several

typical Si/TiO_2 composite reported by other literature. It was shown that the electrochemical performance of our designed 3D $Si/TiO_x/C$ composite electrode presents well comparable with other typical structure Si/TiO_x composites. The excellent rate capability of 3D $Si/TiO_x/C$ is ascribed to the following aspects. Firstly, the porous conductive matrix possesses abundant void space to alleviate the expansion of Si during cycling. Secondly, the 3D continuous conducting scaffold structures directly connected to the current collector, thus providing channels for fast electron transport. Thirdly, Polycrystalline TiO_2 reacts with Li^+ at the first cycle to form Li_xTiO_2, which provides a highly stable SEI layer and promotes the electron/Li-ion path in the during the cycles.

To illustrate the reasons of excellent electrochemical performance for porous $Si/TiO_x/C$ composite electrode, the morphology and composition of $Si/TiO_x/C$ before and after the first cycling were examined by TEM and HRTEM. TEM images of $Si/TiO_x/C$ reveal the 3D morphology of $Si/TiO_x/C$ (Figure 6a), displaying a full coverage of nanoparticles with a size of around 50 nm encapsulated in 3D scaffold. EDX spectrum in Figure S4 conforms the presence of Si, Ti, C and O components in $Si/TiO_x/C$. The HRTEM of $Si/TiO_x/C$ further demonstrates that the Si nanoparticle was coated with an amorphous layer with thickness about 10 nm (Figure 6b). The SEAD pattern of $Si/TiO_x/C$ is identified to be (111), (220), (400) planes, indicating single crystalline for the Si. A ring pattern corresponding to the (101) plane of anatase TiO_2 is observed, indicating that polycrystalline TiO_2 formed at low temperature treatment. The result is corresponded with the XRD pattern of $Si/TiO_x/C$. After the first cycle, the cell was discharged to 0.01 V. Then the composite electrode was disassembled and active materials were scraped from current collector and tested using HRTEM system. Interestingly, as shown in Figure 6d, the morphology of $Si/TiO_x/C$ after cycling is significantly different from original $Si/TiO_x/C$. The single-crystal diffraction pattern of Si can no longer be found in the SEAD pattern of the $Si/TiO_x/C$ composite electrode as Si nanoparticles become amorphous after the first cycle at full lithiation state (Figure 6e). Meanwhile, the SEAD pattern of $Si/TiO_x/C$ after the 1st cycle showed two diffraction rings. The lattice fringe spacing is 0.204 nm and 0.147 nm, corresponding to the (104) and (0010) planes of cubic Li_xTiO_2 (JCPDS

#40-1053). The presence of Li_xTiO_2 indicates that TiO_2 also traps Li ion within the voltage window of 0.01-3.0 V. Therefore, the electrochemical reaction mechanism of Li with $Si/TiO_x/C$ can be described by the following equations:

$$4.4Li + Si \leftrightarrow Li_{4.4}Si \quad (1)$$

$$xLi^+ + xe^- + TiO_2 \rightarrow Li_xTiO_2 \quad (2)$$

Previous reasearch has been confirmed that TiO_2 reacts with Li^+ to form $LiTiO_2$, which enhances the electrical conductivity. Meanwhile, Li_xTiO_2 provides a highly stable SEI layer during the cycles, resulting in excellent electrochemical performances and significantly improved high thermal stability[28, 29].

CV curves were further tested on a half-cell in a potential range between 0.01 and 3.0 V versus Li/Li^+ at a scanning rate of 0.1 mV s^{-1} (Figure 7). In the first cycle, the peak at 0.44 V in the cathodic process corresponds to the formation of SEI layers, which disappears in the second cycle. The sharp reduction peak appears below 0.2 V, representing the lithium reaction with Si (eq 1). After that, an anodic peak is observed at 0.57 V. These two redox peaks correspond to the lithiation/delithiation process of Li with active silicon particles. Moreover, in the profile of $Si/TiO_x/C$ composite electrode, a peak located at 0.62 V in the first reduction scan is attributed to the irreversible electrochemical reduction of the pristine TiO_2 phase and formation of Li_xTiO_2 (eq 2) [56]. The existence of $LiTiO_2$ in the $Si/TiO_x/C$ has been proven to be of good conductivity and is advantageous for electrical pathways similar to the traditional carbon coating on electrode materials for LIBs.

EIS technique was also utilized to clarify the remarkable increased electrochemical performance of Si, Si/C, and $Si/TiO_x/C$ electrodes. Figure 8a displays the Nyquist plots of Si, Si/C, Si/TiO_x and $Si/TiO_x/C$ composite electrodes after 5 cycles (all batteries were tested after 5 cycles at lithiated state). All the Nyquist plots of the electrodes include one depressed semicircle in the high frequency region and a sloped line in the low frequency region. The high frequency semicircle is due to the formation of the SEI film and the charge transfer reaction at the interface of the electrolyte and active materials. The sloping straight line at low frequencies corresponds to the Li ion diffusion in the

electrode. The charge-transfer resistance parameters of the Si/TiO_x/C electrodes are obviously smaller than those of the bare Si ,Si/C and Si/TiO_x electrodes, which indicates it has higher electrical conductivity. In addition, the Nyquist plots of Si/TiOx/C composite electrode after different cycles were also compared in Figure 8b and the corresponding equivalent circuit is presented in insets of Figure 8b. The Nyquist plots are fitted with the equivalent circuit, which consists of an independent electrolyte-electrode resistance (R_e), two resistors: SEI film resistance (R_{sf}) and charge transfer resistance (R_{ct}) with constant phase elements (CPE) in parallel and a Warburg diffusion element. The equivalent circuit parameters obtained from fitting the experimental impedance spectra are listed in Table 2. The R_e of the Si/TiO_x/C composite electrode after the 1st, 5th and 50th cycle are 1.949 Ω, 2.649 Ω and 4.135 Ω, respectively, demonstrating a fast electronic conductivity of Si/TiO_x/C electrode due to the 3D conductive scaffold. Moreover, the R_{sf} after the 1st cycle is 150.7 Ω and stable at the range of 140-150 Ω, which could be attributed to the stable SEI layer formed on the TiO_x/C shell of Si nanoparticles.

The structural stability of Si/TiO_x/C composite electrode was visually verified by SEM images of Si/TiO_x/C after 50 cycles (Figure 9). Compared with the original composite electrode (Figure 9a), the overall surface morphology is conspicuously maintained except for smooth SEI layers formed on the surface of matrix. Continuous conductive matrix structure well encapsulates Si nanoparticles. The cross-section SEM images of Si/TiO_x/C before (Figure 9c) and after cycles (Figure 9d) clearly show that the volume of whole Si/TiO_x/C composite electrode expanded but still maintained integrity after repeated cycling. The thickness of film increased from 10 μm to 16 μm, about ~60% volume exchange. The much smaller volume exchange of Si/TiO_x/C composite electrode compared with Si nanoparticle indicates that the robust 3D conductive scaffold effectively alleviates the expansion of Si during cycling.

As a result, the excellent electrochemical stability of porous Si/TiO_x/C composite electrode is attributed to the unique porous 3D conductive scaffold structure. Firstly, the porous conductive matrix possesses abundant void space to alleviate the large volume expansion of the Si particles

during lithium insertion. Moreover, the formation of Li_xTiO_2/C electrical scaffold structure provides an enhanced electrical conductivity. Meanwhile, the continuous framework helps provide good electrical connection to the Si particles and maintain the structural integrity.

4. Conclusion

The present work demonstrates a facile and scalable solution to fabricate high-performance Si/TiO_x/C composite electrode by embeding Si nanoparticles in a nanostructured 3D porous conductive TiO_x/C framework. By taking advantage of the conductive TiO_x/C framework, which provides fast electronic and ionic transfer channels, as well as porous structure for Si volume changes, the Si/TiO_x/C composite electrode achieved a high capacity and stable cycling performance. The binder free Si/TiO_x/C composite electrode is not only a promising anode for high-performance lithium-ion batteries, but also provides a preferable approach that can be easily extended to other battery electrode material systems that undergo large volume changes and unstable SEI formation during cycling.

Acknowledgements

Financial supported from the 973 project (2013CB934001 and 2015CB932500) and NSF of China (51172024, 51372022 and 51302011) are gratefully acknowledged.

References

1. J. R. Szczech and S. Jin, *Energy Environ. Sci.*, 2011, **4**, 56-72.
2. U. Kasavajjula, C. Wang and A. J. Appleby, *J. Power Sources*, 2007, **163**, 1003-1039.
3. L. Ji, Z. Lin, M. Alcoutlabi and X. Zhang, *Energy Environ. Sci.*, 2011, **4**, 2682-2699.
4. H. Wu and Y. Cui, *Nano Today*, 2012, **7**, 414-429.
5. J. Song, S. Chen, M. Zhou, T. Xu, D. Lv, M. L. Gordin, T. Long, M. Melnyk and D. Wang, *J. Mater. Chem. A*, 2014, **2**, 1257-1262.
6. D. J. Lee, H. Lee, M.-H. Ryou, G.-B. Han, J.-N. Lee, J. Song, J. Choi, K. Y. Cho, Y. M. Lee and J.-K. Park, *ACS Appl. Mater. Interfaces*, 2013, **5**, 12005-12010.
7. L.-F. Cui, R. Ruffo, C. K. Chan, H. Peng and Y. Cui, *Nano Lett.*, 2008, **9**, 491-495.
8. C. K. Chan, H. Peng, G. Liu, K. McIlwrath, X. F. Zhang, R. A. Huggins and Y. Cui, *Nat. Nanotechnol.*, 2008, **3**, 31-35.
9. H. Wu, G. Chan, J. W. Choi, I. Ryu, Y. Yao, M. T. McDowell, S. W. Lee, A. Jackson, Y. Yang and L. Hu, *Nat. Nanotechnol.*, 2012, **7**, 310-315.
10. K. Karki, Y. Zhu, Y. Liu, C.-F. Sun, L. Hu, Y. Wang, C. Wang and J. Cumings, *ACS Nano*, 2013, **7**, 8295-8302.
11. H. Wu, G. Zheng, N. Liu, T. J. Carney, Y. Yang and Y. Cui, *Nano Lett.*, 2012, **12**, 904-909.
12. T. H. Hwang, Y. M. Lee, B.-S. Kong, J.-S. Seo and J. W. Choi, *Nano Lett.*, 2012, **12**, 802-807.
13. N. Liu, H. Wu, M. T. McDowell, Y. Yao, C. Wang and Y. Cui, *Nano Lett.*, 2012, **12**, 3315-3321.
14. B. Wang, X. Li, X. Zhang, B. Luo, Y. Zhang and L. Zhi, *Adv. Mater.*, 2013, **25**, 3560-3565.
15. Z. Zhang, M. Zhang, Y. Wang, Q. Tan, X. Lv, Z. Zhong, H. Li and F. Su, *Nanoscale*, 2013, **5**, 5384-5389.
16. H. Jung, Y.-U. Kim, M.-S. Sung, Y. Hwa, G. Jeong, G.-B. Kim and H.-J. Sohn, *J. Mater. Chem.*, 2011, **21**, 11213-11216.
17. C. Du, M. Chen, L. Wang and G. Yin, *J. Mater. Chem.*, 2011, **21**, 15692-15697.
18. Y. Xu, G. Yin, Y. Ma, P. Zuo and X. Cheng, *J. Mater. Chem.*, 2010, **20**, 3216-3220.
19. R. Yi, F. Dai, M. L. Gordin, S. Chen and D. Wang, *Adv. Energy. Mater.*, 2013, **3**, 295-300.
20. X. Ma, M. Liu, L. Gan, P. K. Tripathi, Y. Zhao, D. Zhu, Z. Xu and L. Chen, *Phys. Chem. Chem. Phys.*, 2014, **16**, 4135-4142.
21. C. Du, C. Gao, G. Yin, M. Chen and L. Wang, *Energy Environ. Sci.*, 2011, **4**, 1037-1042.

22. B. Wang, X. Li, X. Zhang, B. Luo, M. Jin, M. Liang, S. A. Dayeh, S. Picraux and L. Zhi, *ACS Nano*, 2013, **7**, 1437-1445.

23. X. Xin, X. Zhou, F. Wang, X. Yao, X. Xu, Y. Zhu and Z. Liu, *J. Mater. Chem.*, 2012, **22**, 7724-7730.

24. Z. Zhang, Y. Wang, W. Ren, Q. Tan, Y. Chen, H. Li, Z. Zhong and F. Su, *Angew. Chem., Int. Ed.*, 2014, **53**, 5165-5169.

25. L. Zhang, Y. Wang, G. Kan, Z. Zhang, C. Wang, Z. Zhong and F. Su, *RSC Advances*, 2014, **4**, 43114-43120.

26. A. Magasinski, P. Dixon, B. Hertzberg, A. Kvit, J. Ayala and G. Yushin, *Nat. Mater.*, 2010, **9**, 353-358.

27. Y. Park, N.-S. Choi, S. Park, S. H. Woo, S. Sim, B. Y. Jang, S. M. Oh, S. Park, J. Cho and K. T. Lee, *Adv. Energy. Mater.*, 2013, **3**, 206-212.

28. G. Jeong, J.-G. Kim, M.-S. Park, M. Seo, S. M. Hwang, Y.-U. Kim, Y.-J. Kim, J. H. Kim and S. X. Dou, *ACS Nano*, 2014, **8**, 2977-2985.

29. E. M. Lotfabad, P. Kalisvaart, K. Cui, A. Kohandehghan, M. Kupsta, B. Olsen and D. Mitlin, *Phys. Chem. Chem. Phys.*, 2013, **15**, 13646-13657.

30. E. M. Lotfabad, P. Kalisvaart, A. Kohandehghan, K. Cui, M. Kupsta, B. Farbod and D. Mitlin, *J. Mater. Chem. A*, 2014, **2**, 2504-2516.

31. S. Fang, L. Shen, G. Xu, P. Nie, J. Wang, H. Dou and X. Zhang, *ACS Appl. Mater. Interfaces*, 2014, **6**, 6497-6503.

32. J. Brumbarov and J. Kunze-Liebhäuser, *J. Power Sources*, 2014, **258**, 129-133.

33. J. Ye, Y. An, T. Heo, M. Biener, R. Nikolic, M. Tang, H. Jiang and Y. Wang, *J. Power Sources*, 2014, **248**, 447-456.

34. J. Rong, X. Fang, M. Ge, H. Chen, J. Xu and C. Zhou, *Nano Research*, 2013, **6**, 182-190.

35. Z. Wei, R. Li, T. Huang and A. Yu, *J. Power Sources*, 2013, **238**, 165-172.

36. Y. Tang, D. Wu, S. Chen, F. Zhang, J. Jia and X. Feng, *Energy Environ. Sci.*, 2013, **6**, 2447-2451.

37. Q. Wu, T. Tran, W. Lu and J. Wu, *J. Power Sources*, 2014, **258**, 39-45.

38. H. Usui, K. Wasada, M. Shimizu and H. Sakaguchi, *Electrochim. Acta*, 2013, **111**, 575-580.

39. X. Li, Y. Bai, D. Yan, C. Yu, K. Jiang, N. Wan, Q. Wu, S. Sun and W. Zhang, *Mater. Lett.*, 2014, **126**, 295-298.

40. I. Moriguchi, R. Hidaka, H. Yamada, T. Kudo, H. Murakami and N. Nakashima, *Adv. Mater.*, 2006, **18**, 69-73.

41. J.-Y. Shin, J. H. Joo, D. Samuelis and J. Maier, *Chem. Mater.*, 2012, **24**, 543-551.

42. T. Xia, W. Zhang, J. Murowchick, G. Liu and X. Chen, *Nano Lett.*, 2013, **13**, 5289-5296.

43. Z. Hong, M. Wei, T. Lan, L. Jiang and G. Cao, *Energy Environ. Sci.*, 2012, **5**, 5408-5413.

44. H. Xiong, H. Yildirim, E. V. Shevchenko, V. B. Prakapenka, B. Koo, M. D. Slater, M. Balasubramanian, S. K. Sankaranarayanan, J. P. Greeley and S. Tepavcevic, *J. Phys. Chem. C*, 2012, **116**, 3181-3187.

45. J.-Y. Shin, J. H. Joo, D. Samuelis and J. Maier, *Chem. Mater.*, 2012, **24**, 543-551.

46. F. H. Schacher, P. A. Rupar and I. Manners, *Angew. Chem., Int. Ed.*, 2012, **51**, 7898-7921.

47. H. Wu, G. Yu, L. Pan, N. Liu, M. T. McDowell, Z. Bao and Y. Cui, *Nat. Commun.*, 2013, **4**, 1943-1947.

48. C. H. Chen, E. M. Kelder and J. Schoonman, *Thin Solid Films*, 1999, **342**, 35-41.

49. O. Park, J.-I. Lee, M.-J. Chun, J.-T. Yeon, S. Yoo, S. Choi, N.-S. Choi and S. Park, *RSC Advances*, 2013, **3**, 2538-2542.

50. M. N. Obrovac and L. Christensen, *Electrochem. Solid-State Lett.*, 2004, **7**, A93-A96.

51. Y. Hwa, W.-S. Kim, B.-C. Yu, J.-H. Kim, S.-H. Hong and H.-J. Sohn, *J. Electroanal. Chem.*, 2014, **712**, 202-206.

52. M.-S. Wang and L.-Z. Fan, *J. Power Sources*, 2013, **244**, 570-574.

53. A. Naldoni, M. Allieta, S. Santangelo, M. Marelli, F. Fabbri, S. Cappelli, C. L. Bianchi, R. Psaro and V. Dal Santo, *J. Am. Chem. Soc.*, 2012, **134**, 7600-7603.

54. S. T. Myung, M. Kikuchi, C. S. Yoon, H. Yashiro, S. J. Kim, Y. K. Sun and B. Scrosati, *Energy Environ. Sci.*, 2013, **6**, 2609-2614.

55. T. Xia, W. Zhang, J. B. Murowchick, G. Liu and X. B. Chen, *Adv. Energy. Mater.*, 2013, **3**, 1516-1523.

56. L. Aldon, P. Kubiak, A. Picard, J. C. Jumas and J. Olivier-Fourcade, *Chem. Mater.*, 2006, **18**, 1401-1406.

Tables

Table 1 Surface area and porosity of $Si/TiO_x/C$

Sample	S_{Total} $(m^2g^{-1})^a$	S_{meso} $(m^2g^{-2})^b$	S_{micro} $(m^2g^{-2})^c$	V_{total} $(cm^3g^{-1})^d$	V_{meso} $(cm^3g^{-1})^e$	V_{micro} $(cm^3g^{-1})^f$	APD $(nm)^g$
$Si/TiO_x/C$	130.93	127.5	3.43	0.4704	0.47	0.0004	3.8

a) The total surface area (S_{Total}) are derived from the sum of the mesopore areas and micropore area; b) Mesopore areas (S_{meso}) and e) mesopore volume(V_{meso}) are calculated by BJH method; c) Micropore area (S_{micro}) and f) V_{micro} are calculated by SF method; d) Total pore volume (V_{total}) was estimated from the amount adsorbed at a relative pressure P/P_0 of 0.99; g) APD: Average pore diameter are calculated by using BJH model.

Table 2 Equivalent circuit parameters obtained from fitting the experimental impedance spectra

$Si/TiO_x/C$	$R_e(\Omega)$	$R_{sf}(\Omega)$	$R_{ct}(\Omega)$	$W_{dif}(\Omega\ s^{-1/2})$	CPE1(F)	CPE2(F)
After 1 cycle	1.949	150.7	23.26	0.272	1.23E-5	4.33E-6
After 5 cycles	2.649	152.3	29.68	0.258	1.34E-5	4.21E-6
After 50 cycles	4.135	141.8	38.5	0.247	1.24E-5	3.58E-6

Figure captions:

Figure 1. Schematic illustration of preparation the porous Si/TiO_x/C composite electrodes

Figure 2. SEM image of (a) pure Si NPs; (b) Si/TBOT/PMMA film; (c) and (d) Si/TiO_x/C composite electrode.

Figure 3. (a) XRD patterns of Si/TiO_x/C, Si/C, Si NPs and pure TiO_2 calcined at 400°C; (b) XPS spectras of Si/TiO_x/C; core-level XPS spectra of (c)Ti 2p ; (d) O 1s.

Figure 4. (a) Nitrogen adsorption-desorption isotherms and (b) pore size distribution of Si/TiO_x/C.

Figure 5. Electrochemical tests for Si/TiO_x/C: (a) charge-discharge potential profiles of Si/TiO_x/C at different cycles. The cell was measured at 100 mA g^{-1}; (b) the cycling performance of pure TiO_2, Si, Si/C and Si/TiO_x/C electrodes at 100 mA g^{-1} (open: Li insertion, solid: Li extraction); (c) potential profiles of Si/TiO_x/C at different current density in the voltage range of 0.01-1.5 V; (d) delithiation rate capability of Si/TiO_x/C and Si/C.

Figure 6. (a) TEM and (b) HRTEM micrographs of Si/TiO_x/C; (c) SEAD pattern of Si/TiO_x/C; (d) TEM and (e) HRTEM micrographs of Si/TiO_x/C after 1 cycle at lithiation state; (f) SEAD pattern of Si/TiO_x/C after 1 cycle at lithiation state.

Figure 7. (a) the CV of Si/TiO_x/C from 0.01 to 3.0 V at a scan rate of 0.1 mV s^{-1}.

Figure 8 (a) Nyquist plots of Si, Si/C, Si/TiO_x and Si/TiO_x/C composite electrode after 5 cycles at a current density of 200 mA g^{-1}; (b) Nyquist plots of porous Si/TiO_x/C composite electrode after different cycles at a current density of 200 mA g^{-1}; inset Figure 8b is the equivalent circuit used to model the impedance spectra.

Figure 9. (a) and (b) surface and cross section SEM images for Si/TiO_x/C electrode before cycle; (c) and (d) surface and cross section SEM images for Si/TiO_x/C electrode after 50 cycles at charge state with the current density of 100 mA g^{-1}.

456 **Figures:**

457

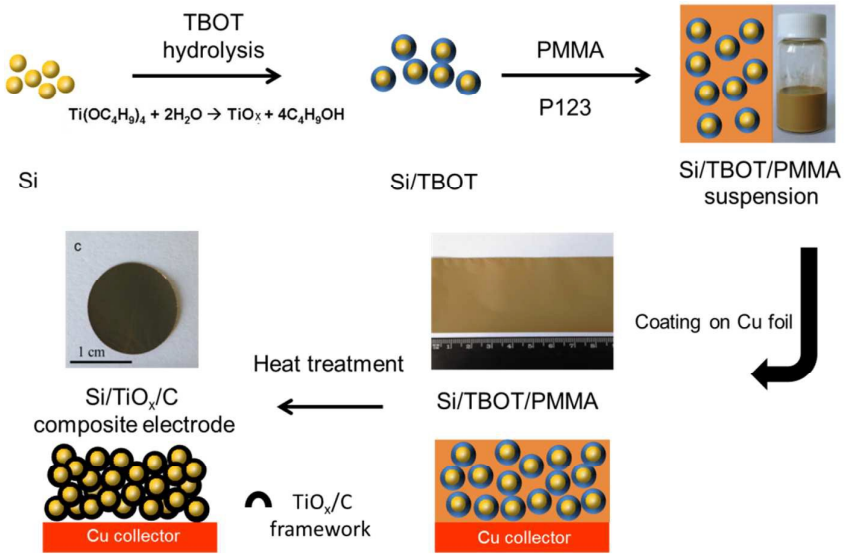

458

459 Figure 1

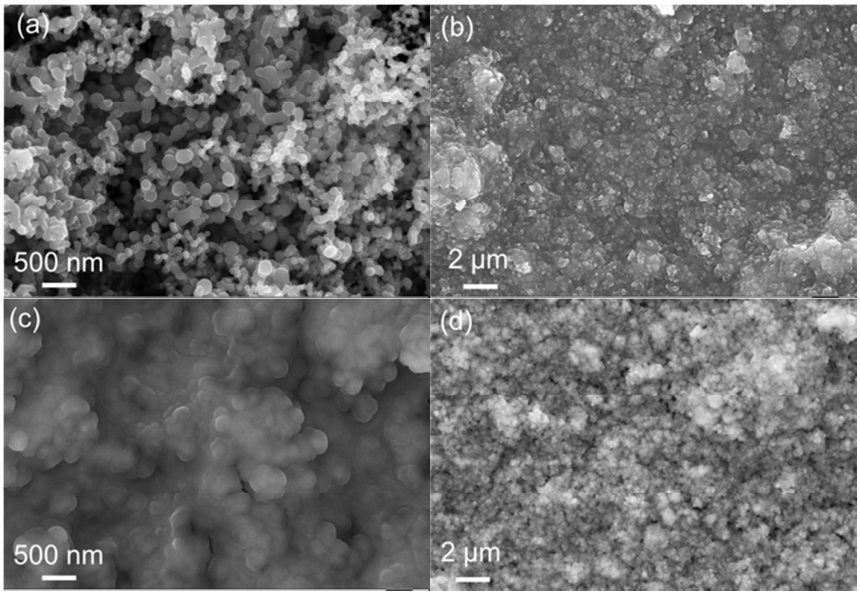

Figure 2

464

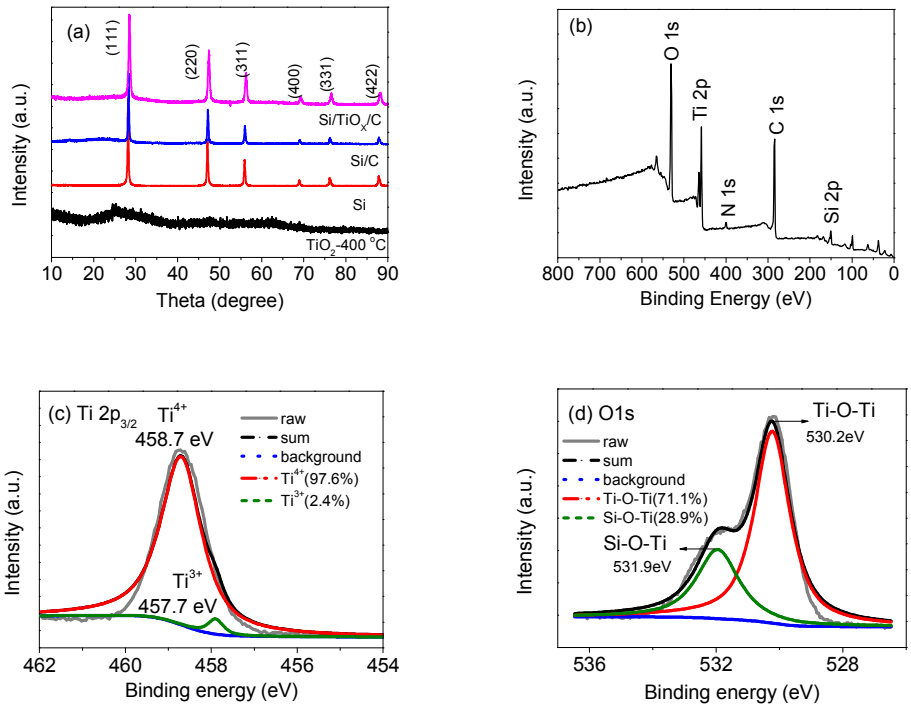

465

466

467

Figure 3

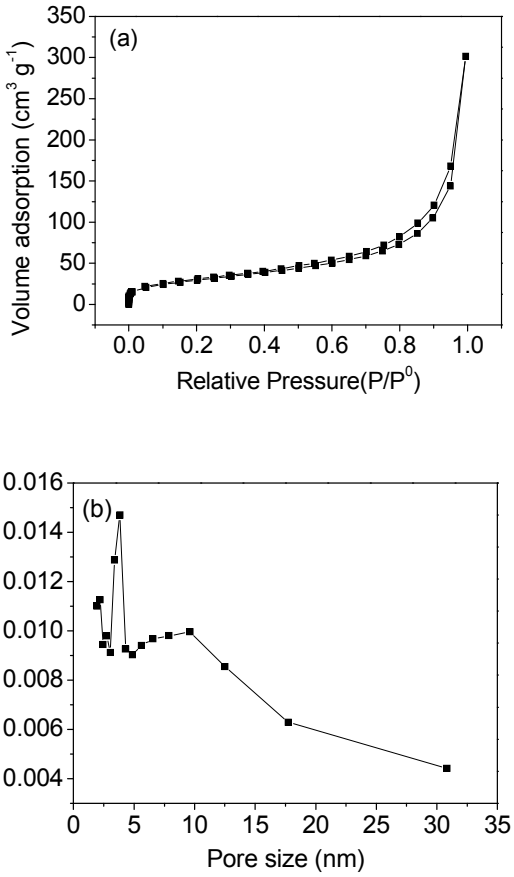

Figure 4

472

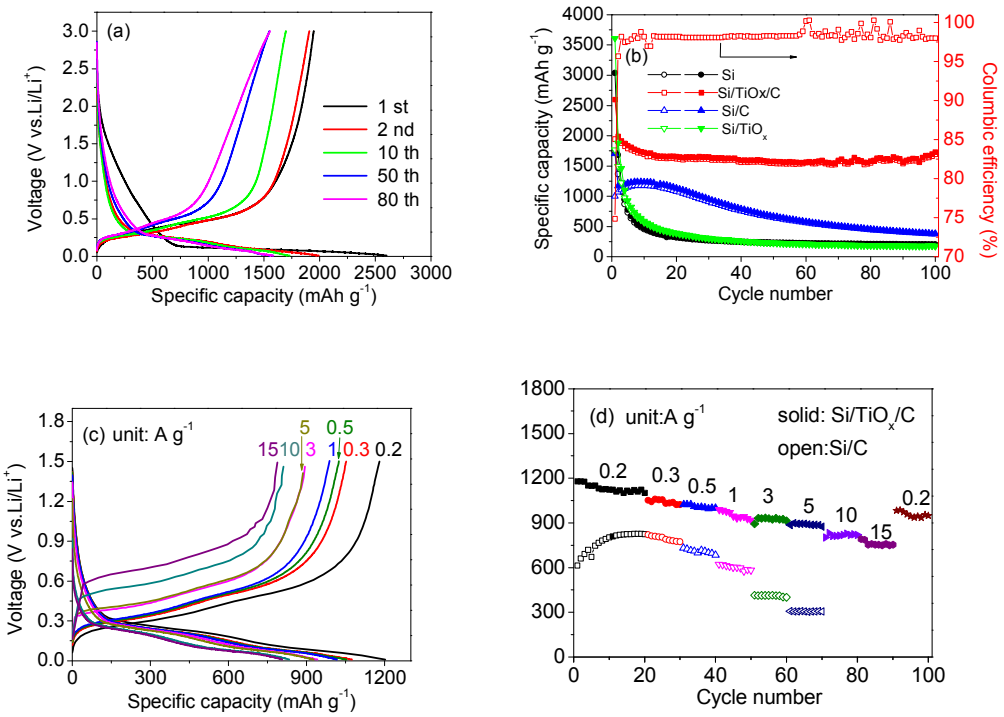

473

474

475 Figure 5

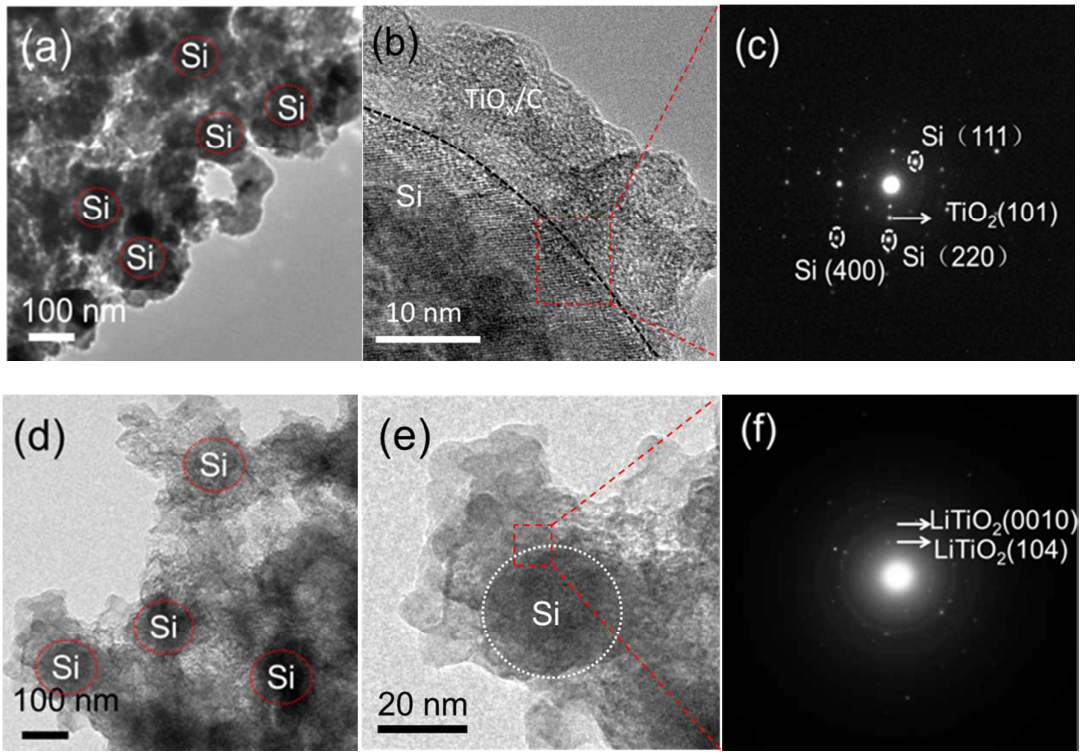

Figure 6

480

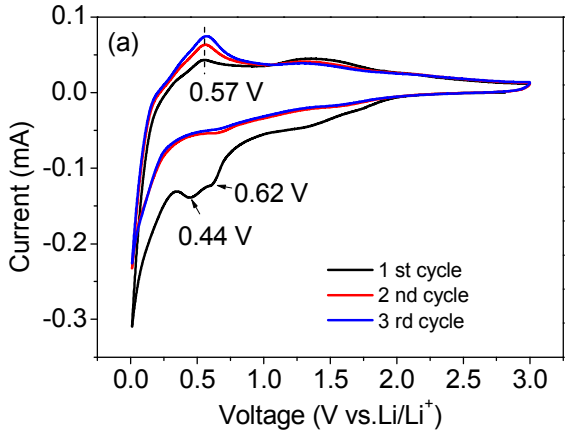

481

482 Figure 7

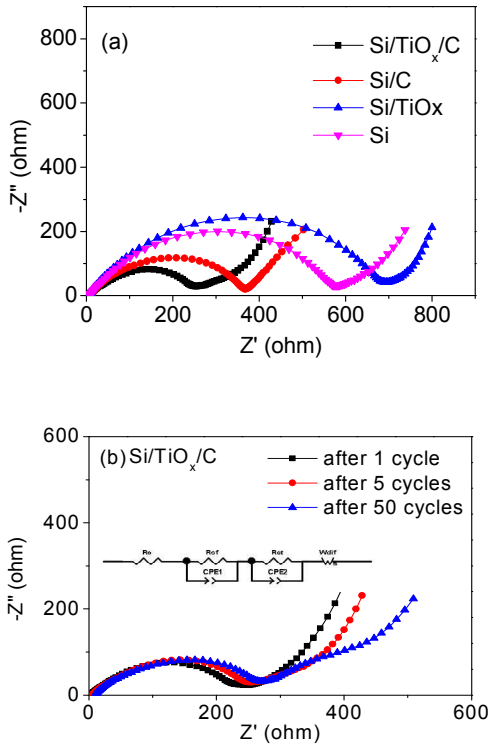

Figure 8

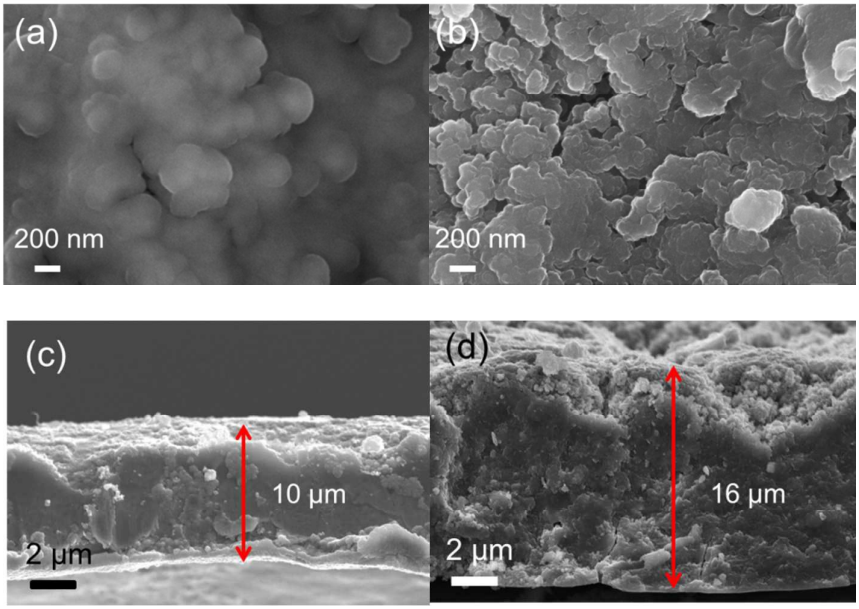

Figure 9

Table of Contents

Unique three-dimensional porous silicon/TiOx/C (Si/TiOx/C) binder free composite electrodes were scalable fabricated. By taking advantage of the conductive TiOx/C frameworks, the Si/TiOx/C electrodes exhibit superior cycling and rate performance.